# High-throughput FCS using an LCOS spatial light modulator and an 8 × 1 SPAD array

**Ryan A. Colyer,[1,3] Giuseppe Scalia,[1] Ivan Rech,[2] Angelo Gulinatti,[2] Massimo Ghioni,[2] Sergio Cova,[2] Shimon Weiss,[1] and Xavier Michalet[1,4]**

[1] *Department of Chemistry & Biochemistry, UCLA, Los Angeles, CA*
[2] *Dipartimento di Elettronica ed Informazione, Politecnico di Milano, Milano, Italy*
[3] *ryancolyer@yahoo.com*
[4] *michalet@chem.ucla.edu*

**Abstract:** We present a novel approach to high-throughput Fluorescence Correlation Spectroscopy (FCS) which enables us to obtain one order of magnitude improvement in acquisition time. Our approach utilizes a liquid crystal on silicon spatial light modulator to generate dynamically adjustable focal spots, and uses an eight-pixel monolithic single-photon avalanche photodiode array. We demonstrate the capabilities of this system by showing FCS of Rhodamine 6G under various viscosities, and by showing that, with proper calibration of each detection channel, one order of magnitude improvement in acquisition speed is obtained. More generally, our approach will allow higher throughput single-molecule studies to be performed.

©2010 Optical Society of America

**OCIS codes:** (300.6280) Spectroscopy: Spectroscopy, fluorescence and luminescence; (300.2530) Spectroscopy: Fluorescence, laser-induced; (180.2520) Microscopy: Fluorescence microscopy; (040.1240) Detectors: Arrays; (040.6070) Detectors: Solid-state detectors; (230.6120) Optical devices: Spatial light modulators

## References and links

1. S. Weiss, "Fluorescence spectroscopy of single biomolecules," Science **283**(5408), 1676–1683 (1999).
2. X. Michalet, S. Weiss, and M. Jäger, "Single-molecule fluorescence studies of protein folding and conformational dynamics," Chem. Rev. **106**(5), 1785–1813 (2006).
3. N. L. Thompson, "Fluorescence Correlation Spectroscopy," in *Topics in Fluorescence Spectroscopy, Vol 1: Techniques*, J.R. Lakowicz, ed. (Plenum Press, New York, 1991).
4. O. Krichevsky, and G. Bonnet, "Fluorescence correlation spectroscopy: the technique and its applications," Rep. Prog. Phys. **65**(2), 251–297 (2002).
5. E. Haustein, and P. Schwille, "Fluorescence correlation spectroscopy: novel variations of an established technique," Annu. Rev. Biophys. Biomol. Struct. **36**(1), 151–169 (2007).
6. M. Gösch, H. Blom, S. Anderegg, K. Korn, P. Thyberg, M. Wells, T. Lasser, R. Rigler, A. Magnusson, and S. Hård, "Parallel dual-color fluorescence cross-correlation spectroscopy using diffractive optical elements," J. Biomed. Opt. **10**(5), 054008 (2005).
7. M. Gösch, A. Serov, T. Anhut, T. Lasser, A. Rochas, P.-A. Besse, R. S. Popovic, H. Blom, and R. Rigler, "Parallel single molecule detection with a fully integrated single-photon 2x2 CMOS detector array," J. Biomed. Opt. **9**(5), 913–921 (2004).
8. M. Burkhardt, and P. Schwille, "Electron multiplying CCD based detection for spatially resolved fluorescence correlation spectroscopy," Opt. Express **14**(12), 5013–5020 (2006).
9. D. R. Sisan, R. Arevalo, C. Graves, R. McAllister, and J. S. Urbach, "Spatially resolved fluorescence correlation spectroscopy using a spinning disk confocal microscope," Biophys. J. **91**(11), 4241–4252 (2006).
10. B. Kannan, L. Guo, T. Sudhaharan, S. Ahmed, I. Maruyama, and T. Wohland, "Spatially resolved total internal reflection fluorescence correlation microscopy using an electron multiplying charge-coupled device camera," Anal. Chem. **79**(12), 4463–4470 (2007).
11. B. Kannan, J. Y. Har, P. Liu, I. Maruyama, J. L. Ding, and T. Wohland, "Electron multiplying charge-coupled device camera based fluorescence correlation spectroscopy," Anal. Chem. **78**(10), 3444–3451 (2006).
12. T. Wohland, X. Shi, J. Sankaran, and E. H. K. Stelzer, "Single plane illumination fluorescence correlation spectroscopy (SPIM-FCS) probes inhomogeneous three-dimensional environments," Opt. Express **18**(10), 10627–10641 (2010).
13. F. Guerrieri, S. Tisa, A. Tosi, and F. Zappa, "Two-dimensional SPAD imaging camera for photon counting," IEEE Photonics Journal **2**(5), 759–774 (2010).

14. C. Niclass, C. Favi, T. Kluter, M. Gersbach, and E. Charbon, "A 128 x 128 single-photon image sensor with column-level 10-bit time-to-digital converter array," IEEE J. Solid-state Circuits **43**(12), 2977–2989 (2008).
15. C. Niclass, A. Rochas, P. A. Besse, R. Popovic, and E. Charbon, "A 4 mu s integration time imager based on CMOS single photon avalanche diode technology," Sens. Actuators A Phys. **130-131**, 273–281 (2006).
16. I. Rech, D. Resnati, S. Marangoni, M. Ghioni, and S. Cova, "Compact-eight channel photon counting module with monolithic array detector," Proc. SPIE **6771**, 677113 (2007).
17. E. R. Dufresne, G. C. Spalding, M. T. Dearing, S. A. Sheets, and D. G. Grier, "Computer-generated holographic optical tweezer arrays," Rev. Sci. Instrum. **72**(3), 1810–1816 (2001).
18. H. Dai, K. Xu Y. Liu, X. Wang, and J. Liu, "Characteristics of LCoS phase-only spatial light modulator and its applications," Opt. Commun. **238**(4-6), 269–276 (2004).
19. X. W. Wang, H. Dai, and K. Xu, "Tunable reflective lens array based on liquid crystal on silicon," Opt. Express **13**(2), 352–357 (2005).
20. M. Polin, K. Ladavac, S. H. Lee, Y. Roichman, and D. G. Grier, "Optimized holographic optical traps," Opt. Express **13**(15), 5831–5845 (2005).
21. X. Michalet, A. Cheng, J. Antelman, M. Suyama, K. Arisaka, and S. Weiss, "Hybrid photodetector for single-molecule spectroscopy and microscopy," Proc. SPIE **6862**, 68620F (2008).
22. I. Rech, S. Marangoni, D. Resnati, M. Ghioni, and S. Cova, "Multipixel single-photon avalanche diode array for parallel photon counting applications," J. Mod. Opt. **56**(2), 326–333 (2009).
23. T. A. Laurence, S. Fore, and T. Huser, "Fast, flexible algorithm for calculating photon correlations," Opt. Lett. **31**(6), 829–831 (2006).
24. M. J. Culbertson, and D. L. Burden, "A distributed algorithm for multi-tau autocorrelation," Rev. Sci. Instrum. **78**(4), 044102 (2007).
25. D. N. Fittinghoff, P. W. Wiseman, and J. A. Squier, "Widefield multiphoton and temporally decorrelated multifocal multiphoton microscopy," Opt. Express **7**(8), 273–279 (2000).
26. J. Bewersdorf, R. Pick, and S. W. Hell, "Multifocal multiphoton microscopy," Opt. Lett. **23**(9), 655–657 (1998).
27. A. H. Buist, M. Müller, J. A. Squier, and G. J. Brakenhoff, "Real time two-photon absorption microscopy using multipoint excitation," J. Microsc. **192**(2), 217–226 (1998).
28. R. Heintzmann, Q. S. Hanley, D. Arndt-Jovin, and T. M. Jovin, "A dual path programmable array microscope (PAM): simultaneous acquisition of conjugate and non-conjugate images," J. Microsc. **204**(2), 119–135 (2001).
29. M. Reicherter, T. Haist, E. U. Wagemann, and H. J. Tiziani, "Optical particle trapping with computer-generated holograms written on a liquid-crystal display," Opt. Lett. **24**(9), 608–610 (1999).
30. R. A. Colyer, G. Scalia, T. Kim, I. Rech, D. Resnati, S. Marangoni, M. Ghioni, S. Cova, S. Weiss, and X. Michalet, "High-throughput multispot single-molecule spectroscopy," Proc. SPIE **7571**, 75710G (2010).
31. M. Polin, K. Ladavac, S. H. Lee, Y. Roichman, and D. G. Grier, "Optimized holographic optical traps," Opt. Express **13**(15), 5831–5845 (2005).
32. M. Born, and E. Wolf, *Principles of Optics: Electromagnetic Theory of Propagation, Interference and Diffraction of Light*. 7th ed. (Cambridge University Press, Cambridge, 1999).
33. D. R. Lide, ed., *CRC Handbook of Chemistry & Physics*. 82 ed. (CRC Press. 2001–2002), p. 2664.
34. C. B. Müller, A. Loman, V. Pacheco, F. Koberling, D. Willbold, W. Richtering, and J. Enderlein, "Precise measurement of diffusion by multi-color dual-focus fluorescence correlation spectroscopy," Europhys. Lett. **83**(4), 46001 (2008).
35. P. Kask, R. Günther, and P. Axhausen, "Statistical accuracy in fluorescence fluctuation experiments," Eur. Biophys. J. **25**(3), 163–169 (1997).
36. H. Qian, "On the statistics of fluorescence correlation spectroscopy," Biophys. Chem. **38**(1-2), 49–57 (1990).
37. S. Saffarian, and E. L. Elson, "Statistical analysis of fluorescence correlation spectroscopy: the standard deviation and bias," Biophys. J. **84**(3), 2030–2042 (2003).
38. R. Verberk, and M. Orrit, "Photon statistics in the fluorescence of single molecules and nanocrystals: correlation functions versus distributions of on- and off-times," J. Chem. Phys. **119**(4), 2214–2222 (2003).
39. T. Wohland, R. Rigler, and H. Vogel, "The standard deviation in fluorescence correlation spectroscopy," Biophys. J. **80**(6), 2987–2999 (2001).
40. X. Michalet, T. D. Lacoste, and S. Weiss, "Ultrahigh-resolution colocalization of spectrally separable point-like fluorescent probes," Methods **25**(1), 87–102 (2001).
41. A. N. Kapanidis, E. Margeat, T. A. Laurence, S. Doose, S. O. Ho, J. Mukhopadhyay, E. Kortkhonjia, V. Mekler, R. H. Ebright, and S. Weiss, "Retention of transcription initiation factor sigma70 in transcription elongation: single-molecule analysis," Mol. Cell **20**(3), 347–356 (2005).
42. S. Weiss, "Measuring conformational dynamics of biomolecules by single molecule fluorescence spectroscopy," Nat. Struct. Biol. **7**(9), 724–729 (2000).

## 1. Introduction

Single-molecule fluorescence techniques are powerful tools for observing molecular conformations, interactions, concentrations, and motion [1,2] but since they must operate at the single-molecule level, they generally require long acquisitions to acquire adequate statistics. Fluorescence Correlation Spectroscopy (FCS) is the simplest of such technique and

is commonly used to observe binding interactions or the diffusion of fluorescent particles in vitro or in vivo [3–5]. To monitor the signal fluctuations due to changes in the number of particles entering or leaving the focal volume, FCS measurements need to be performed at concentrations that are neither too low (in order to obtain enough signal during the finite duration of the measurement) nor too high (to still be able to observe sizable number fluctuations above the total shot noise). In practice, FCS is generally performed at nanomolar concentrations with typical acquisition times on the order of a few seconds to several minutes. A typical geometry for this kind of measurements is the confocal geometry, in which a microscopic volume in a solution is illuminated with a tightly focused laser beam [4].

Increased FCS throughput is desirable for two different reasons. In high-content screening approaches, one is interested in monitoring the effect of many different small molecules (e.g. drugs) on a reaction or molecular conformation. The goal is to obtain a rapid answer to many different "reactions". It is best achieved in a parallel (multi-well) geometry, in which different reactions take place at different locations and need to be interrogated simultaneously. In its typical confocal implementation, FCS is not easily parallelizable, not the least because the best detectors, namely single-photon avalanche photodiodes (SPADs) are bulky and expensive. Therefore multi-well FCS entails successive interrogation of each well, which results in a total measurement time proportional to the number of wells. Similar issues arise when trying to probe different locations in a cell using confocal FCS in order to map diffusion or binding interactions [5].

Another situation in which high-throughput FCS (HT-FCS) would be desirable is when observing fast evolving dynamic systems. In this case, the minimum duration of an FCS measurement needed to obtain statistically significant results sets the maximum temporal resolution. In other words, if it takes 10 seconds to obtain a useful FCS measurement, phenomena evolving with a time constant shorter than 10 seconds will not be resolvable. A solution to this problem is to acquire the same kind of data from several distinct locations in the same sample and pool the data together in order to obtain the same statistics in a shorter amount of time.

In the recent past, several approaches have been proposed to increase the throughput of FCS measurements. Past approaches trying to use several SPADs were limited by cost and bulkiness, but also revealed the critical need of obtaining close to perfect multi-spot excitation patterns matching the detector arrangements [6,7]. More recently, signal detection using ultrasensitive cameras has been proposed, using either a confocal excitation scheme [8,9] or a widefield excitation scheme [10–12]. Although promising, these approaches have limited temporal resolution due to the finite frame rate of current cameras and are therefore limited to slow diffusion processes such as those encountered in live cells.

With the advent of high-performance SPAD arrays [13–16], HT-FCS (and in general high-throughput single-molecule spectroscopy) becomes achievable. We present here our first results towards this goal. We used a liquid crystal on silicon spatial light modulator (LCOS-SLM) to generate an array of excitation spots and a multi-pixel monolithic single-photon avalanche photodiode (SPAD) array to detect the corresponding individual signals. The resulting large amount of data is acquired using an FPGA-based acquisition board and processed using custom software able to time-stamp each photon with 12.5 ns resolution in all channels in parallel.

After describing our method to generate multiple excitation spots with an LCOS-SLM, the corresponding optical setup, and our data acquisition algorithms, we present results demonstrating the capabilities of this combination. Multichannel FCS data analysis of Rhodamine 6G (R6G) in solutions with various viscosities illustrates our ability to calibrate each channel and to measure subtle changes in small molecule diffusion due to varying environment. Finally, we illustrate the high-throughput capabilities of our approach by showing that FCS data can be acquired one order of magnitude faster than previously by pooling together data from all channels.

## 2. Materials and Methods

### 2.1 Multispot generation using an LCOS-SLM

To obtain precise control over the generation of multiple excitation spots, we used a liquid crystal on silicon spatial light modulator (LCOS-SLM or in short, LCOS, X10468-01, Hamamatsu, Bridgewater, NJ). This unit allows arbitrarily adjusting the number, positions and size of the generated spots as explained below. LCOS devices change the phase of the light they reflect on a pixel-by-pixel basis. They are typically used in the spatial-frequency domain, the phase pattern imposed by the device being the Fourier transform of the desired intensity distribution pattern in real space. Computation of these patterns is generally iterative and time-consuming [17]. In contrast, our approach uses the LCOS in the real-space domain, to generate a real-space array of spots at an intermediate focal plane in front of the LCOS (see Fig. 3 below). Real-space approaches to spot formation with an LCOS have been done previously using a Fresnel zone plate [18], and also with an approach mathematically similar to our own, but in a non-microscopy setup [19]. In our approach, relay optics recollimate the intermediate point sources generated by the LCOS, and the spots are then focused into the sample using a microscope objective lens. This method has two main advantages: the user can straightforwardly define the desired pattern and modify it instantaneously, and it allows rejecting specular reflections from the LCOS which would contribute to background illumination. To compute the necessary LCOS pattern, we use the Huygens-Fresnel principle: using a distinct region of $n \times n$ pixels of the LCOS for each generated spot, we look for a pattern of phase delays that redirects each ray reflected by each pixel towards a single point in front of the LCOS.
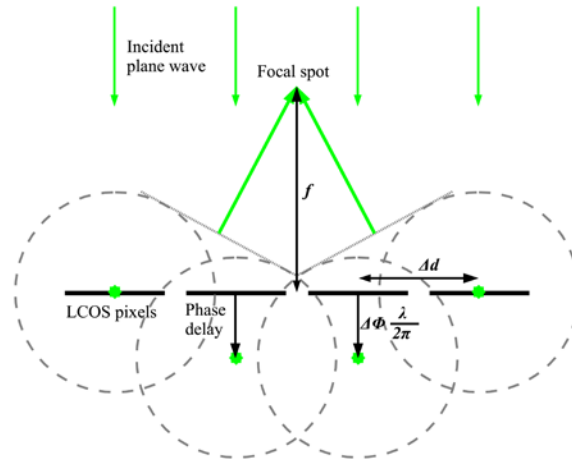


Fig. 1. A schematic showing how the Huygens-Fresnel principle can be used to determine the desired phase delay at each point. Rays interfere constructively at a focal point when they all have the same total phase delay due to distance and phase delay applied by the LCOS.

From simple geometric considerations, (see Fig. 1), the desired relative phase delay, $\Delta\varphi$, between neighboring pixels is given to first order by:

$$\Delta\varphi = \frac{-2\pi \mathrm{d}\Delta d}{\lambda f} \qquad (1)$$

where $d = \sqrt{x^2 + y^2}$ is the distance of a pixel from the center of the pattern, $\lambda$ is the wavelength, and $f$ is the desired focal distance. Integrating Eq. (1) over the LCOS pixels used

to generate a single spot, the desired phase delay pattern for a single focal spot is given, similarly to Wang et al. [19], as:

$$\varphi = \pi \left( 2 - \frac{d^2}{\lambda f} \right) \qquad (2)$$

Multiple focal spots can then be generated by repeating this pattern periodically, according to the number and arrangement of the desired spots (Fig. 2). Since this pattern is generated by a simple algebraic expression, it is very easy to compute any periodic pattern with arbitrary spacing, spatial offset, number of focal spots, focal distance or angle of the pattern, making it ideal as an approach for interactive or automatic alignment of multiple spots.

The area outside of the pattern used to generate the spots can be set to a constant phase value (represented by solid black in Fig. 2), so that the reflected light from this region retains the plane wave characteristics of the incident light. When passing through the recollimating lens (Fig. 3), this unmodified part of the reflected light is focused to a point, and can be easily filtered out by a small opaque pindot [20]. In contrast, the spots generated by the rest of the LCOS pattern are each transformed by the recollimating lens into as many collimated plane waves (each with a slightly different phase angle), and are thus unaffected by the pindot. Therefore only the generated focal spots continue on into the back aperture of the objective. The rejection of the specular reflection component of the LCOS (showing up as a zero-mode spot in the spatial-frequency methods) is an important capability of our approach because regardless of the LCOS pattern, there always exists a fraction of specular reflection for which the phase is not modulated. Our spatial pattern approach, combined with the use of a pindot, allows the selective removal of this specular reflection, resulting in high contrast and no diffuse illumination regions generated by the fraction of light with no phase modulation.
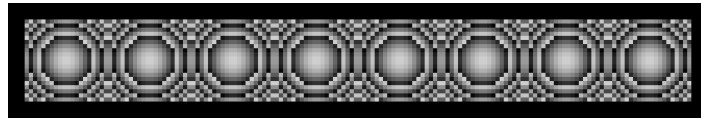


Fig. 2. Example LCOS pattern with a 20 pixel pitch used to generate 8x1 spots. Each pixel represents 20 μm on the LCOS screen. Gray levels correspond to the range available on the LCOS, and go from 0 (black) to 209 (pale gray) corresponding to a phase delay of $2\pi$.

We developed custom software using LabVIEW (National Instruments – NI, Austin, TX) for interactive generation of multi-spot patterns according to user-specified parameters (number of spots in X and Y, pitch, focal distance, offset and rotation angle). The user interface permits straightforward and instantaneous adjustments of the generated spot pattern, greatly simplifying the alignment of detectors as discussed below.

*2.2 Microscopy setup*

The collimated light of a 532 nm emitting 8 ps pulsed laser (IC-532-1000 ps, High Q Laser, Rankweil, Austria) was expanded and directed toward the LCOS-SLM to form an array of illumination spots in an intermediate image plane located at $f$ = 15 mm from the device's window (Fig. 3). The resulting light beams were then reflected by a mirror, sent to a recollimating lens, filtered by a pindot to remove the specular reflection and re-imaged into the sample with a 60X, NA = 1.2, water immersion objective lens (UPlan Apo, Olympus, Center Valley, PA), generating near-diffraction limited spots.

Fluorescence emitted by the sample was collected by the same objective lens and passed through a 532 LP dichroic mirror LPD01-532RU-25x36x1.1, Semrock, Rochester, NY), a 532 LP sharp edge filter (LP03-532RU-25, Semrock). Relay optics and a bandpass filter adapted to the emission spectrum of R6G (single band band-pass 582DF75 filter, FF01-

582/75-25, Semrock) completed the emission path. A pair of achromatic lenses was used to adjust image magnification to match the pixel spacing on the SPAD array detector.

### 2.3 Setup alignment

An 8x1 spot pattern was generated using the LCOS-SLM as described above. The pitch of the LCOS pattern was set so that the total active area captured much of the expanded laser light while still having a flat field of illumination. Fine adjustment of the emission path magnification to match the SPAD array was performed using a CCD camera placed at the same location where the SPAD array was located during data acquisition. Using a concentrated 1.8 μM solution of R6G excited by the LCOS pattern, we focused the excitation pattern onto the surface (covered with a uniform layer of adsorbed R6G molecules). We then adjusted the positioning of the lenses in the emission path until the CCD camera showed all spots in focus and with the correct distance between spots in the detector image plane, thus fixing the relationship between magnification (spot spacing) and focus.

Once the proper spot separation was obtained, the CCD camera was removed, and the SPAD array was placed in the same position. There are 4 degrees of freedom to adjust in this procedure: X, Y, Z and tilt angle. The first three were adjusted as follows: limiting the LCOS pattern to a single central spot, we moved the SPAD array in X, Y and Z in order to maximize the recorded intensity detected by the corresponding center SPAD. Next, the LCOS pattern was adjusted to move the single spot to one edge pixel and then its opposite to determine if the outer spots corresponded to the outer pixels. The Z position of the detector was adjusted until an optimal match was obtained. Each edge spot of the LCOS pattern was then moved in X and Y to maximize the signal collected by each edge pixel. Using this information, trigonometry was used to determine a new pattern rotation angle optimizing the alignment. This Z translation and angle adjustment procedure was iterated a few times until convergence.
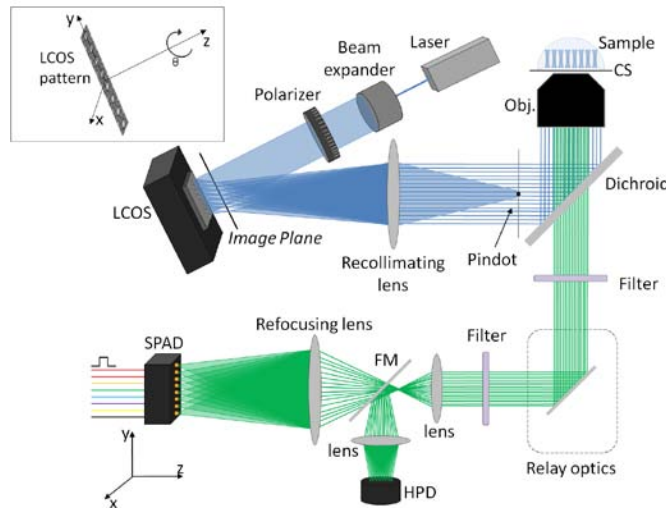


Fig. 3. Schematic of the experimental setup using an LCOS-SLM. Blue lines represent the excitation light path. Green lines represent the emission light path towards the detectors (HPD for excitation profile measurements and SPAD array for FCS measurements). A first array of spots is generated in an intermediate image plane in front of the LCOS. A recollimating lens sends this pattern to the back of an objective lens, which focuses it into the sample. CS: Coverslip, Obj: objective lens, FM: flippable mirror. Top left inset: LCOS pattern degrees of freedom controllable by software. The pattern pitch can also be adjusted.

*2.4 Excitation and emission PSF measurement*

Excitation point spread functions (PSFs) were measured using stage-scanning confocal imaging of a single subdiffraction sized fluorescent bead using a single-pixel hybrid photodetector (HPD) (Model R7110U-40UF, Hamamatsu Photonics, Bridgewater, NJ) as described in [21] for single spot excitation. Briefly, the 8x1 LCOS pattern was turned on and the bead was raster-scanned in the XY and YZ directions through these 8 excitation spots, while the single pixel HPD recorded the emitted fluorescence intensity. Since the bead transited through 8 distinct excitation spots, the detector recorded 8 distinct regions of excitation, whose spacing reflected the excitation PSFs separation in the sample plane. Since the HPD sensitive area (Ø 3 mm) was larger than the projected image of the eight spots (~1.75 mm), the total emitted intensity was recorded without any clipping, thus reflecting the excitation energy density in the sample plane (excitation PSF).

In contrast, the emission PSF corresponding to the SPAD cannot be directly recorded. However, repeating the procedure described previously using the SPAD array instead of the HPD, the product of the excitation and emission PSFs for each spot was obtained.

*2.5 Detectors and data acquisition system*

We used a custom-CMOS linear array of single-photon avalanche photodiodes (SPAD array or SPADA) described in [22]. The SPAD circular sensitive area has a diameter of 50 µm and is separated from its nearest neighbor by 250 µm (center-to-center distance). Each SPAD is wire-bounded to a dedicated active quenching and pulse shaping circuit, outputting a 50 ns wide TTL pulse. A DB15 connector at the back of the housing gives access to all 8 TTL pulse trains. We used a DB15 to 8 BNC cable to connect each channel to a breakout box (model CA-1000, NI), supporting 16 connections (i.e. 2 SPADA modules). The breakout box inputs were sent to the first 16 inputs of a reconfigurable digital input/output (I/O) board (model PXI-7813R, NI) supporting up to 160 inputs. Data from the board are transferred to the host computer via a PXI-PCI communication bridge (PXI-1000B crate, PXI-8830 MXI-3 board, PCI-8830/8335 board, NI).

The Virtex-II 3M Field Programmable Gate Array (FPGA) at the core of the PXI-7813R board was programmed using LabVIEW FPGA using a simple pipelined architecture. Briefly, a timed-loop running at 80 MHz increments a single 32 bits counter and checks for a down/up transition on each channel. Upon detection of a pulse, the counter value is passed to a local First in First out (FIFO) buffer (one FIFO per channel, 1028 words depth). Concurrently, a timed pipelined loop (80 MHz) reads each channel FIFO sequentially, and passes the channel number followed by the counter value to a Direct Memory Access (DMA) transfer FIFO (32 KWords). This unsophisticated architecture sustains up to 200 kcps on 8 channels. On the host computer, a program written in LabVIEW reads the data transferred to the DMA FIFO and can process it during or after acquisition. For instance, data can be streamed to disk, binned and represented as an intensity time trace. Data files can be read to compute autocorrelation and cross-correlation functions using published algorithms [23,24].

*2.6 Fluorescence correlation spectroscopy*

Autocorrelation functions (ACFs) of the individual channel's signal fluctuations were calculated in either of the following ways: (i) using a fast Fourier transform (FFT) algorithm, (ii) a multitau algorithm based on binned time traces [24], or (iii) a multitau algorithm based on photon time-stamps [23].

The time-dependence of the SPAD afterpulsing contribution was estimated using constant white light illumination (Fig. 4), in which case afterpulsing dominates the measured ACFs. The afterpulsing contribution to the ACFs appears well described by a power law (though the exponent depends on which channel is considered) and was therefore taken into account by introducing a power law component when fitting experimental data as described next.
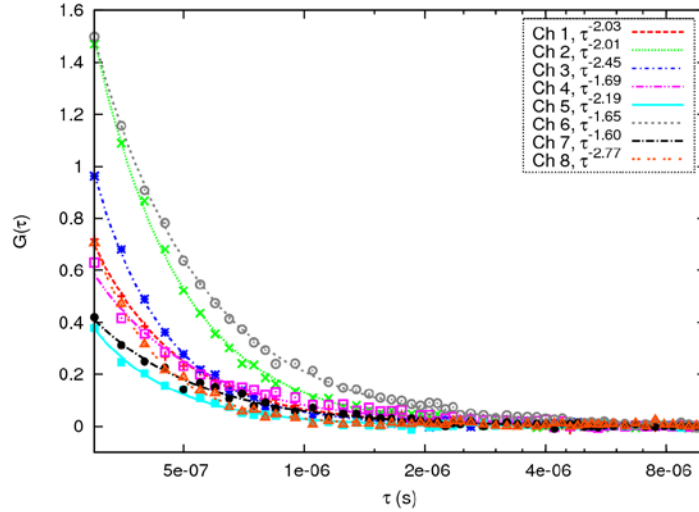
Fig. 4. Autocorrelation functions of white light at 30kcps showing the afterpulsing behavior of each channel. The fits shown are power law functions. The exact amplitude depends on the count rate and is therefore channel-dependent.

The $k^{th}$ channel's ACF $G_k(\tau)$ ($k = 1,\ldots, 8$) for a sample with $S$ diffusing species $i = 1,\ldots, S$ was fitted to a multicomponent, background-corrected, 2D diffusion model including a power law afterpulsing term [3]:

$$G_k(\tau) = A_k \tau^{b_k} + \gamma_k \left(1 - \frac{B_k}{I_k}\right)^2 \frac{\sum_{i=1}^{S} \left(\alpha_k^{(i)}\right)^2 N_k^{(i)} \left(1 + 4D^{(i)}\tau / w_{k,xy}^2\right)^{-1}}{\left(\sum_{i=1}^{S} \alpha_k^{(i)} N_k^{(i)}\right)^2} \qquad (3)$$

where $A_k$ and $b_k$ are coefficients describing the amplitude and exponent of the $k^{th}$ channel afterpulsing component, respectively. $\gamma_k$ is a geometric factor characterizing the excitation/detection volume:

$$\gamma_k = \frac{\oint_{\Omega} d\vec{r} \left[X_k(\vec{r}) D_k(\vec{r})\right]^2}{\oint_{\Omega} d\vec{r} X_k(\vec{r}) D_k(\vec{r})}, \qquad (4)$$

where $X_k(\vec{r})$ is the normalized excitation 3D profile ($X_k(0) = 1$) and $D_k(\vec{r})$ is the normalized detection 3D profile ($D_k(0) = 1$) [3]. $I_k$ is the total count rate of the measurement, $B_k$ is the count rate of the uncorrelated background (typically obtained by measuring just the buffer), $w_{k,xy}$ is the Gaussian beam waist in the sample focal plane, and $\alpha_k^{(i)}$, $D^{(i)}$, and $N_k^{(i)}$ are the brightness, diffusion coefficient, and number of molecules per excitation/detection volume for each molecular species $i$ in channel $k$ (the diffusion coefficient $D^{(i)}$ is channel independent). While the free diffusion in the data below is technically 3D diffusion, the $z$ dimensions of the PSFs are much longer than the $x$ and $y$ dimensions, and thus the diffusion is very well-approximated by a 2D diffusion model. The 3D model introduces an additional parameter but with no change in the fitted concentrations

or diffusion rates, no increase in fit quality, and no improvement in the residuals. For equal brightness components ( $\alpha_k^{(i)} = \alpha_k$ ), Eq. (3) simplifies and we obtain:

$$G_k\left(\tau\right) = A_k \tau^{b_k} + \frac{\displaystyle\sum_{i=1}^{S} n_k^{(i)}\left(1+\tau/d_k^{(i)}\right)^{-1}}{\left(\displaystyle\sum_{i=1}^{S} n_k^{(i)}\right)^{2}} \tag{5}$$

where we have introduced the notations:

$$d_k^{(i)} = \frac{w_{k,xy}^2}{4D^{(i)}}$$

$$n_k^{(i)} = \gamma_k^{-1}\left(1-\frac{B_k}{I_k}\right)^{-2} N_k^{(i)}. \tag{6}$$

$n_k^{(0)}$ is proportional to the concentration $C^{(0)}$, defining the effective sampling volume of the $k^{th}$ excitation/detection spot, $V_k$:

$$\gamma_k^{-1} N_k^{(i)} = C^{(i)} V_k \tag{7}$$

and $d_k^{(i)}$ represents the characteristic diffusion time of species $i$ through the $k^{th}$ sampling volume. Fits to Eq. (5) were performed using custom software written in LabVIEW or Gnuplot. In practice, we fixed the exponent $b_k = -1.5$ for all channels, as the values of other parameters of interest ( $n_k^{(i)}$ and $d_k^{(i)}$ ) were found to depend very little on its exact value.

### 2.7 Channel calibration

In single-channel FCS, obtaining quantitative results for the number concentration, $N$, requires the knowledge of $\gamma$, a geometrical characteristic of the excitation/emission PSF [3], as well as correcting for the background contribution $B$. Computation of the diffusion coefficient, $D$, requires knowing the beam waist parameter $w_{xy}$. An identical requirement exists in multi-channel FCS except that these calibration parameters are different for each channel $k$, with each channel having slightly different excitation and emission PSFs and background rates.

   The following steps describe a simple calibration procedure based on a single measurement of a reference sample:

1. Acquire ACFs of a reference sample (indicated by a (0) superscript in the following) with known concentration $C^{(0)}$ and diffusion coefficient $D^{(0)}$. The measurements are performed at signal rate $I_k^{(0)}$ and background rate $B_k^{(0)}$ for each channel $k$. Note that the background rate can be obtained using a pure buffer sample.

2. Perform ACF fits for each channel $k$ of the reference sample, according to Eq. (5) to obtain $n_k^{(0)}$ and $d_k^{(0)}$ .

3. $w_{k,xy}$ and $\gamma_k^{-1} N_k^{(0)}$ can then be obtained from Eq. (6) ($i = 0$) using the known value of $D^{(0)}$. The sampling volume $V_k$ follows from Eq. (7) and the known value of $C^{(0)}$

4. For a new sample with signal and background rate $I_k$ and $B_k$, each ACF can be fitted to Eq. (5) in order to obtain an estimates for each species parameters $n_k^{(i)}$ and $d_k^{(i)}$. The diffusion coefficient $D_k^{(i)}$ and concentration $C_k^{(i)}$ estimated from each channel's ACF fit are then obtained as:

$$D_k^{(i)} = \frac{w_{k,xy}^2}{4d_k^{(i)}} = \frac{d_k^{(0)}}{d_k^{(i)}} D^{(0)}$$

$$C_k^{(i)} = \frac{\rho_k}{\rho_k^{(0)}} \frac{n_k^{(i)}}{n_k^{(0)}} C^{(0)}$$

(8)

Where we have introduced the notations:

$$\rho_k = \left(1 - \frac{B_k}{I_k}\right)^2 ; \quad \rho_k^{(0)} = \left(1 - \frac{B_k^{(0)}}{I_k^{(0)}}\right)^2 .$$

(9)

Ideally, all $D_k^{(i)} = D^{(i)}$ and all $C_k^{(i)} = C^{(i)}$.

5. Alternatively, each channel's ACF can be rescaled in both time and amplitude dimension to compute an "average" ACF for all channels, the latter curve being then fit to Eq. (5). The scaling factors for each channel are defined by:

$$\beta_k = \frac{d_k^{(0)}}{\left\langle d_k^{(0)} \right\rangle_k}$$

$$g_k = \frac{n_k^{(0)}}{\left\langle n_k^{(0)} \right\rangle_k} \frac{\rho_k^{(0)}}{\rho_k}.$$

(10)

where $<...>_k$ indicates an average over all channels. The rescaled ACFs are defined by interpolation of the experimental curves by:

$$\hat{G}_k(\tau) = g_k G_k(\beta_k \tau).$$

(11)

6. After averaging all interpolated curves $\hat{G}_k(\tau)$, the resulting averaged ACF $\hat{G}(\tau)$ can be fitted to Eq. (5), obtaining the fit parameters $\hat{n}^{(i)}$ and $\hat{d}^{(i)}$ verifying:

$$\hat{n}^{(i)} = \frac{C^{(i)}}{C^{(0)}} \left\langle n_k^{(0)} \right\rangle_k$$

$$\hat{d}^{(i)} = \frac{\left\langle w_{k,xy}^2 \right\rangle_k}{4D^{(i)}}.$$

(12)

Note that the ability to compute a scaled and averaged ACF relies on the fact that sample-dependent parameters (concentration, $C^{(i)}$, brightness, $\alpha^{(i)}$, and diffusion time, $d^{(i)}$) are separable from channel-dependent parameters (geometry, $\gamma_k$ and volume, $V_k$) in Eq. (3). This separability allows the correction of the channel-dependent parameters by a simple scaling factor while not disrupting the data describing the sample (even for multi-species samples).

Similarly, since the only occurrence of $\tau$ is in ratio with $d_k^{(i)}$, a correction for the beam waist can be applied as a $d$ scaling factor on $\tau$ without disrupting the functional form of the underlying data. Since the afterpulsing is described by a power law which is by definition scale invariant, both the $n$ scaling and $d$ scaling result in only a change in the amplitude of the afterpulsing component, and do not alter its functional form.

In this work, a single species was used, therefore the index *(i)* will be omitted.

*2.8 Samples*

100 nm diameter fluorescent beads (Fluosphere 540/560, Invitrogen,Carlsbad, CA,) were spin coated on a coverslip at low density to measure excitation and emission PSFs.

For FCS calibration and viscosities measurement we used Rhodamine 6G (590) purchased from Exciton (Dayton, Ohio) diluted in 200 mM NaCl buffer combined with 0%, 10%, 20%, 30%, or 40% sucrose (%w/w) for various viscosities. Fluorophore concentrations were determined by absorption spectrometry using a UV-Vis spectrometer (Lambda 25, Perkin Elmer Instruments, Waltham, MA).

## 3. Results

### 3.1 LCOS generation of a multispot excitation pattern

Multispot confocal microscopy is challenging for several reasons. First, one needs to generate uniform and diffraction-limited excitation spots in the sample. Second, when using a multipixel detector, the pixel arrangement of the detector needs to be reliably aligned with the excitation pattern. Finally, it is desirable that this process be simple, robust, reproducible and adjustable if different laser sources or samples with different spectra are used. A number of solutions have been proposed in the past, including cascaded beam-splitters [25], microlens arrays [26,27], micro-mirror arrays [28] or LCOS spatial light modulators (SLM) [29].

Our initial attempts using a microlens array yielded encouraging results [30] but did not meet the requirement of simple and reliable alignment. To achieve this objective, we chose to use an LCOS-SLM in direct space. LCOS-SLMs are traditionally used in reciprocal space to generate phase-only holograms or kinoforms (e.g. for optical trapping) [29,31]. This approach requires iterative pattern optimization and is sensitive to a number of optical parameters (such as the input laser wave front, optical elements imperfections, etc). Instead, we use the LCOS-SLM as an array of Fresnel lenses. Following the Huygens-Fresnel principle, each pixel $(x, y)$ of the LCOS reflecting the incident laser plane wave acts as the source of a spherical wave with added phase delay $\varphi(x, y)$ interfering with all the others at a common focal plane located at a distance $f_{LCOS}$ from the LCOS array. Using the appropriate phase delay pattern, the resulting intermediate image of spots can be recollimated and sent into the microscope objective lens to generate a demagnified spot pattern in the sample focal plane. Conceptually, our approach is equivalent to a programmable micro-mirror array. Simulations were used to assess the maximum theoretical quality using ideal optical elements and ideal alignment conditions. This allowed evaluating problems due to diffraction limitations and discretization introduced by the finite pixel size of the LCOS. The well-known expression for the maximum angular resolution for a Fresnel lens of diameter $p$ is:

$$\sin(\theta) = 1.22 \frac{\lambda}{p} \tag{13}$$

By trigonometry, setting the angular resolution in the focal plane equal to the lens diameter yields the diffraction-limited maximum focal distance, $f_{max}$ for the focal plane distance from the LCOS:

$$f_{max} = \frac{p^2}{1.22\lambda} \qquad (14)$$

where $\lambda$ is the wavelength, and $p$ is the pattern pitch at the focal plane. For focal distances less than $f_{max}$, simulations showed decreased broadening of the generated focal spot as the focal distance is reduced away from $f_{max}$. To avoid this diffraction induced broadening of the focal spots we were motivated to choose the smallest focal distance permissible by the physical constraints of the device.

We also evaluated pixelization effects and found that, theoretically, patterns generated by a region as small as $3 \times 3$ pixels can still produce reasonable focal spots. Practically, however, bleedthrough of the electric field applied to one pixel into neighboring pixels prevents from achieving acceptable patterns using less than $5 \times 5$ pixels per spot. This same issue of electric field bleedthrough prevents one from using sharp gradients and sets a constraint on the minimal focal distance that can be achieved. For extremely small focal distances, the required phase pattern (modulo $2\pi$) contains sharp phase transitions which upon bleedthrough result in a distorted pattern. To resolve this, we chose focal distances which were smaller than the diffraction maximum, but large enough that the displayed phase pattern contains gradual transitions. For example, for a pattern pitch of 400 μm (20 LCOS pixels of 20 μm each), the diffraction limit for 532 nm light is 75 mm, so we use a pitch of 15 mm.

### 3.2 Point-spread function characterization

To assess the quality of the resulting excitation focal spots, we imaged sub-diffraction sized fluorescent beads (100 nm diameter) using stage–scanning microscopy. To be able to collect light emitted when the bead passed through the distinct excitation spots, we used a large area hybrid photon detector (HPD, diameter = 3 mm) covering the image of the whole excitation pattern in the detection plane. XY and YZ cross-sections of the 8 generated excitation point spread functions (PSFs) are shown in Fig. 5, demonstrating good uniformity of the pattern.

The relevant PSFs for FCS measurements depend on the product of the excitation and emission PSFs. This product can be easily obtained using the same setup, but replacing the HPD with the $8 \times 1$ SPAD array, as shown in Fig. 3. Comparison of the excitation PSFs, measured with the HPD, and the corresponding excitation/detection PSFs, measured with the SPAD array, shows the spatial filtering effect due to the small sensitive area of each SPAD, resulting in rejection of out-of-focus light and clipping of the excitation PSF's "wings". Aberrations are visible in the PSF profiles which can be partially attributed to discretization effects from the finite pixel size of the LCOS, and to imperfections in the LCOS representing the applied phase pattern. Tilt of the outer PSFs with respect to the optical axis is due to the increasing angle of incidence of the plane waves generated by the recollimating lens for outer LCOS spot patterns. It can in principle be minimized by reducing the extent of the LCOS pattern or increasing the focal length of the recollimating focusing lens. In practice, it has a limited impact on FCS measurements in the range of spot number and separations used in this work.

Gaussian fit parameters of the measured PSF profiles (shown in Fig. 6) are reported in Table 1. These parameters are about twice as large as the diffraction limited sizes and perfectly adequate for FCS measurements. A comparison of the spot separations from Fig. 6 and the beam waists from Table 1 shows that the spots are well enough separated to make correlations with neighboring spots very small, such that the spots provide independent measurements, as verified by cross-correlation measurements between neighboring channels (data not shown).
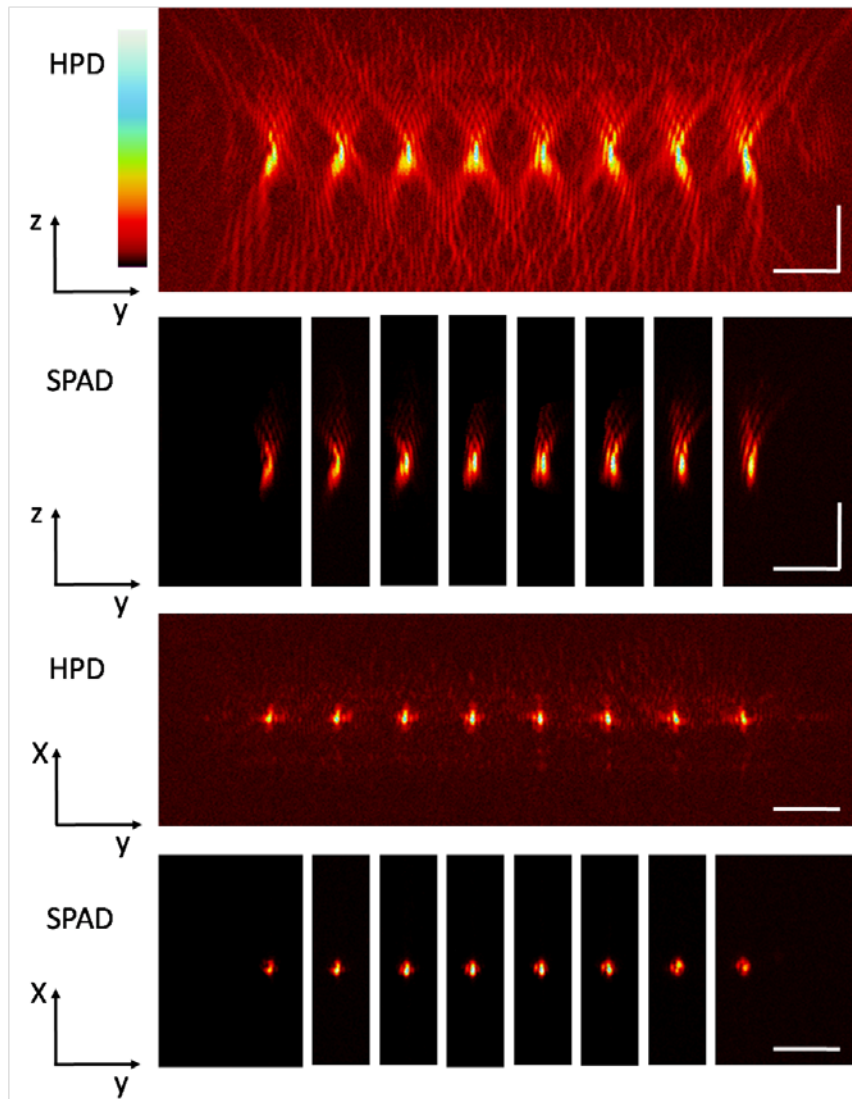
Fig. 5. Intensity maps of the 8 × 1 excitation spot pattern in the directions along (YZ) and perpendicular (XY) the optical axis. The profiles were recorded by stage scanning microscopy of an isolated 100 nm diameter bead using two different detectors, a wide active area single pixel (HPD), and a 8 × 1 SPAD array (SPAD). The same intensity scale was used in all images, where black = 0, red = 110, and white = 1100 counts. Scale bars are 5 µm.
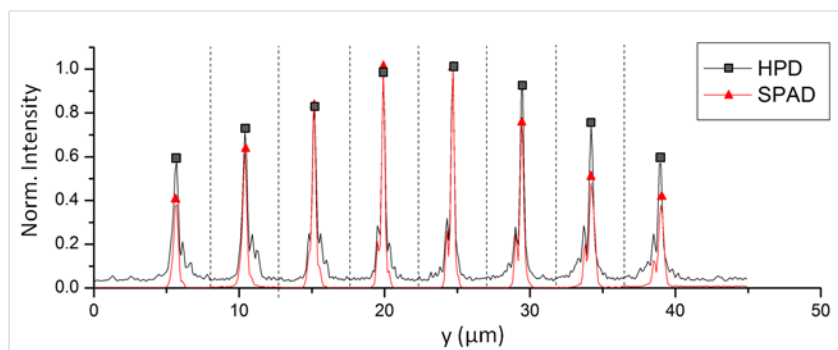
Fig. 6. Comparison between excitation (HPD) and excitation + detection (SPAD) bead scan profiles along the Y axis. The plot shows the clipping of the tails and background reduction for each peak in the SPAD measurement compared to the HPD, at the expense of an intensity loss in the outer channels.

**Table 1. Excitation PSF characteristics. Beam-waist values $w_{xy}$ and $w_z$ were obtained by Gaussian fits of the PSF images acquired by XY and YZ scanning, respectively ($w_{xy}$ is the geometric mean of the waists in both X and Y directions). The excitation PSFs were imaged using a single-pixel HPD while the excitation + detection PSFs were imaged using the $8 \times 1$ SPAD array. All: mean and standard deviation of all spots, Diffr: diffraction limit for the setup characteristics [32].**

| Channel | Excitation | | | Excitation + Detection | | |
|---|---|---|---|---|---|---|
| | $w_{xy}$ (µm) | $w_z$ (µm) | $w_z/w_{xy}$ | $w_{xy}$ (µm) | $w_z$ (µm) | $w_z/w_{xy}$ |
| 1 | 0.43 | 1.93 | 4.5 | 0.42 | 1.28 | 3.0 |
| 2 | 0.37 | 1.52 | 4.1 | 0.37 | 1.11 | 3.0 |
| 3 | 0.34 | 1.35 | 3.9 | 0.36 | 1.04 | 2.9 |
| 4 | 0.34 | 1.35 | 4.0 | 0.30 | 1.12 | 3.8 |
| 5 | 0.36 | 1.37 | 3.8 | 0.33 | 1.11 | 3.4 |
| 6 | 0.39 | 1.39 | 3.6 | 0.34 | 1.30 | 3.9 |
| 7 | 0.39 | 1.70 | 4.3 | 0.38 | 1.34 | 3.5 |
| 8 | 0.42 | 1.55 | 3.7 | 0.36 | 1.56 | 4.3 |
| All | $0.38 \pm 0.03$ | $1.52 \pm 0.21$ | $4.0 \pm 0.3$ | $0.36 \pm 0.04$ | $1.23 \pm 0.17$ | $3.5 \pm 0.5$ |
| Diffr | 0.19 | 0.53 | 2.8 | - | - | - |

*3.3 Multispot FCS experiments*

In order to test the capability of our setup for FCS experiments, we first asked whether we could reliably measure the diffusion coefficient of molecules in solution *for each spot*, $D_k$. Ultimately, we would like to verify that this value does not depend on which channel is used to measure it. Since extracting diffusion coefficients from an FCS measurement involves determining the geometrical parameter $w_{k,xy}$ of each spot $k$ (Eq. (6)), an equivalent question is whether, using a known sample as a calibration sample, the measured diffusion times of different samples scale up according to their known diffusion coefficients. A simple way to obtain such a series is to observe the same molecule in solvents of increasing viscosities. The Stokes-Einstein equation relates the diffusion coefficient $D$ of a molecule to the viscosity $\eta$ of its solvent by:

$$D = \frac{k_B T}{6\pi\eta r} \tag{15}$$

where $k_B$ is the Boltzmann constant, $T$ the absolute temperature and $r$ the molecule's hydrodynamic radius. Equivalently, the diffusion time $d$ (Eq. (6)) increases linearly with the solvent's viscosity. Experimentally, a simple way to increase the viscosity of an aqueous buffer is to add large soluble molecules to it such as sucrose, which has a well characterized effect on the viscosity of water. We prepared samples of 1 nM of Rhodamine 6G (R6G) in buffers of varying viscosity, obtained by using 0%, 10%, 20%, 30%, and 40% sucrose, and performed simultaneous FCS measurements in 8 channels using the $8 \times 1$ SPAD array.

Figure 7 shows a representative FCS curve for one of the channels (channel 4) at 0% sucrose concentration, as well as a fit to a 2D diffusion model (Eq. (5) with a single component). The fit residuals for all channels are shown on the same Fig. and demonstrate the appropriateness of the model for this experiment.
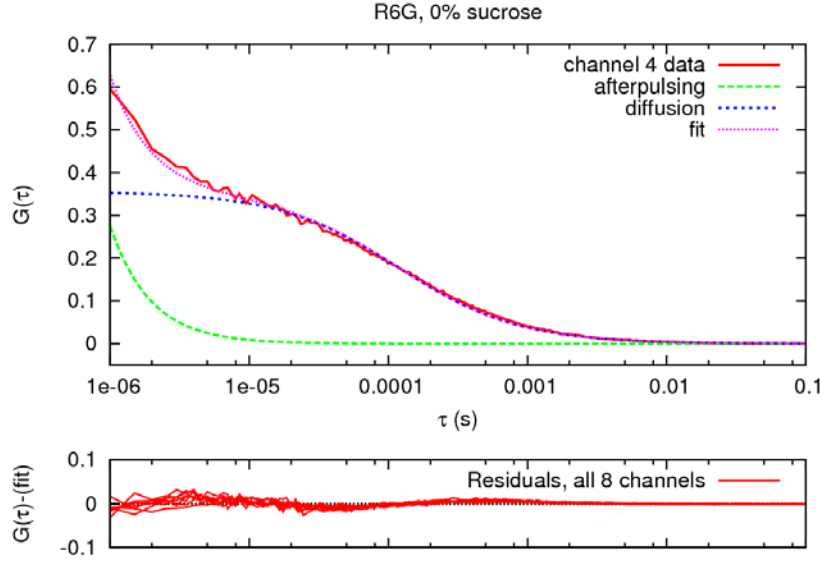


Fig. 7. Representative ACF and fit for R6G in 0% sucrose (channel 4). Fit residuals for all 8 channels are shown in the lower panel. The remaining small residuals are due to the slightly non-Gaussian aspects of the PSFs, as seen in Figs. 5 and 6.

Similar results were obtained with all sucrose concentrations. The results of these experiments are summarized in Fig. 8, which shows the diffusion times $d$ extracted for each sucrose concentration and each channel as a function of the corresponding viscosity [33]. As expected a linear relationship between $d$ and $\eta$ is observed. For a given viscosity $\eta$, slightly different values of the diffusion time $d_{k,\eta}$ are recovered for different channels $k$, as expected from their different geometrical factor $w_{k,xy}$. To show that the difference in diffusion time has a purely geometrical origin, we plotted the different ratios $d_{k,\eta}/\eta$ obtained for all measurements on a channel by channel basis ($k$). According to Eq. (6) and (15):

$$\frac{d_{k,\eta}}{\eta} = \frac{3\pi r}{2k_B T} w_{k,xy}^2 \qquad (16)$$

only depends on the channel parameter $w_{k,xy}$, which is confirmed by Fig. 9a.

These results confirm that it is possible to reliably compute the geometrical characteristic $w_{k,xy}$ of each channel using a single known sample, thus allowing extracting the absolute

diffusion coefficients for unknown samples measured in different experiments, independently of the channel used for the measurement.
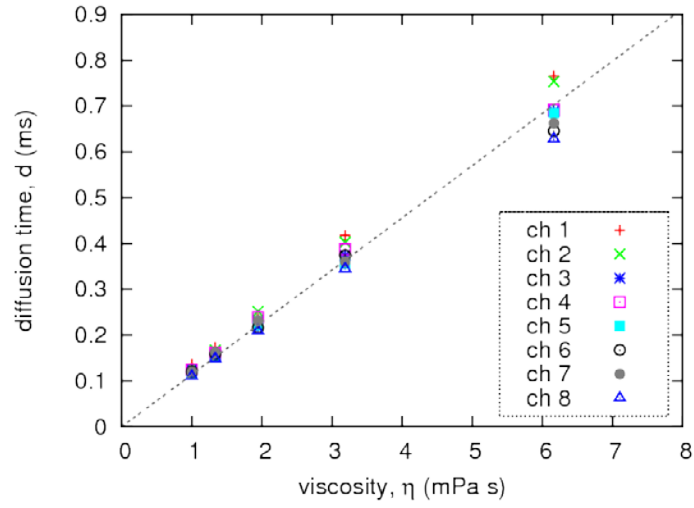


Fig. 8. R6G diffusion time as a function of viscosity for buffers with 0%, 10%, 20%, 30%, and 40% sucrose. A linear relationship (dashed line) is the expected result.
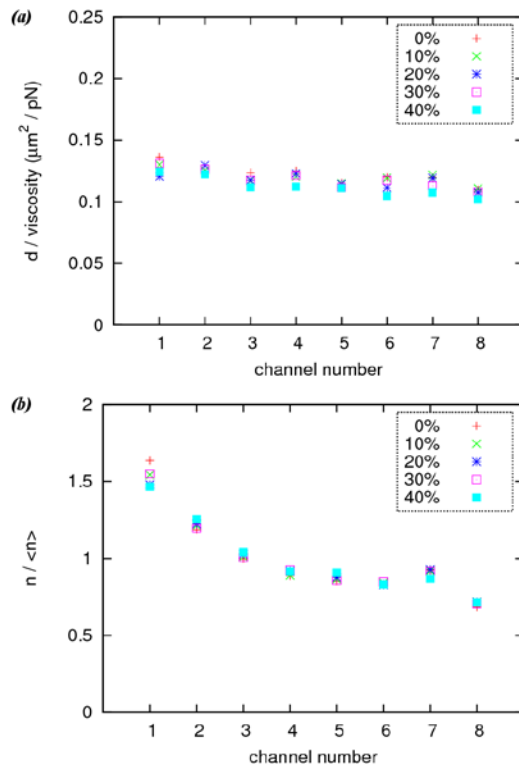


Fig. 9. Channel dependences for the viscosity series of (a) $d/\eta$ and (b) $n/<n>$ (where for each viscosity value, $<n>$ is averaged across the 8 channels).

Next, we asked whether we could reliably extract the concentration information $C_k$ of diffusing molecules *for each spot*. According to Eq. (7), $C_k$ depends in a non-trivial manner on the fit parameter $n_k$, the signal-to-background ratio (SBR) $I_k/B_k$ of the measurement and some fixed geometrical parameters of the channel ($\gamma_k$ and $V_k$). However, assuming that the measurements are all performed in conditions of high SBR, the fitted parameter $n_k$ depends only (linearly) on $C_k$ and some channel-specific geometrical parameter. We thus expect that the $n_k^{(i)}$ normalized by its average value across $M$ measurements of different samples:

$$\left\langle n_k^{(i)} \right\rangle_i = \frac{1}{M} \sum_{i=1}^{M} n_k^{(i)} \tag{17}$$

will have a constant value $\hat{n}_k = n_k^{(i)} \Big/ \left\langle n_k^{(i)} \right\rangle_i$ for each channel. This is indeed what is observed for the viscosity series, as shown in Fig. 9b, demonstrating that a calibration of the concentration is equally possible using a sample of known concentration to extract the geometrical parameter $V_k$ of each channel. The $n_k^{(i)} \Big/ \left\langle n_k^{(i)} \right\rangle_i$ values of Fig. 9b show a greater spread from one channel to the next than the diffusion times shown in Fig. 9a. This is because alignment differences result in a greater variability of PSF volume than PSF width.

These results demonstrate that each FCS channel can be calibrated independently, thus enabling parallel acquisition of FCS data on 8 channels. Channel calibration can be exploited to speed up FCS data acquisition by pooling together data from all 8 channels. We explored this approach using the procedure described in Material and Methods. Briefly, the idea consists of rescaling each individual channel's autocorrelation curve along both time and amplitude axes, and averaging all curves before fitting.

We demonstrate this approach using a sample of 1 nM R6G in 0% sucrose as our calibration sample. This allows us to compute the calibration factors for each channel. Next, we apply these calibration factors to the ACF curves obtained for all of the samples (1 nM R6G in 0%, 10%, 20%, 30%, and 40% sucrose) shown in Fig. 10a. As expected, the uncalibrated curves exhibit significant dispersion across channels for a given sample. After calibration, however, the corrected ACF curves collapse nicely around a single curve, as shown in Fig. 10b. The observed residual differences between the calibrated ACF amplitudes of the five samples are compatible with sample preparation uncertainty. The residual dispersion observed for the largest sucrose concentrations might be due to refraction index effects not taken into account in our calibration procedure.

After averaging the ACF curves of all channels, each sample yields a single 8-channel (8ch) averaged ACF curve shown in Fig. 11a. This 8ch-averaged curve can then be fitted to the same 2D diffusion model used previously, recovering the expected $D_\eta = 1/\eta$ dependence of the diffusion coefficient predicted by Eq. (15) (Fig. 11b).
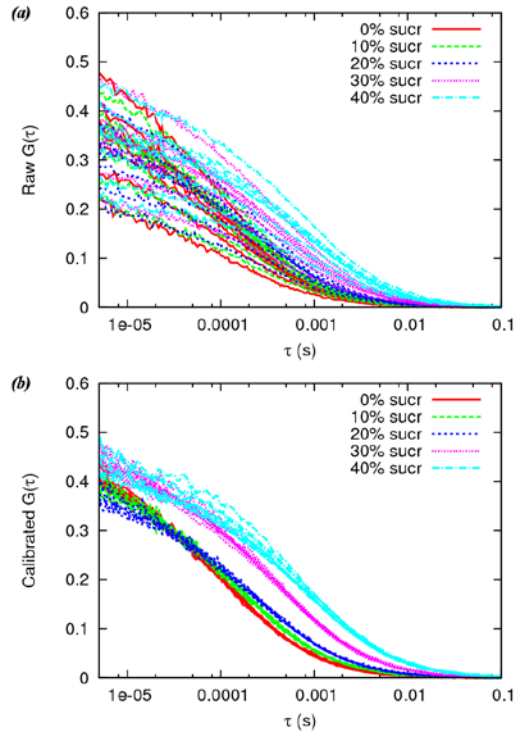
Fig. 10. The calibration process is demonstrated using the R6G 0% sample as a reference, where (a) shows the raw uncalibrated curves, and (b) shows the result of the calibration.
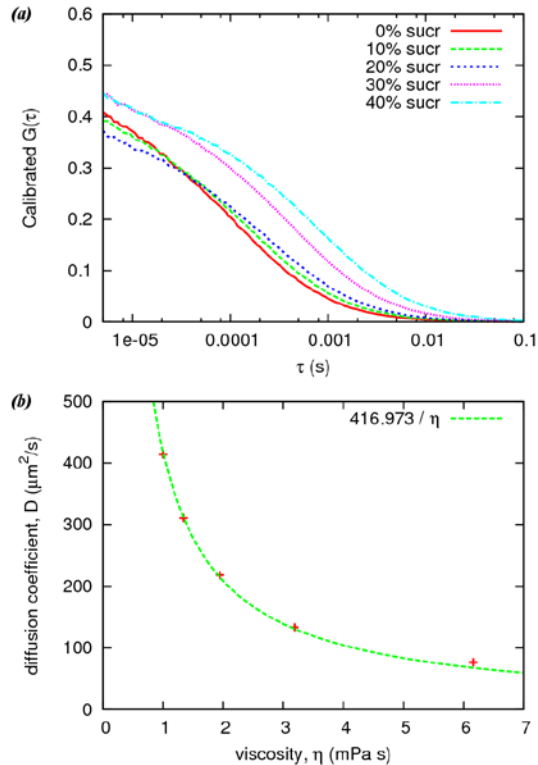
Fig. 11. (a) Calibrated ACF curves obtained from 8 channels for 1 nM R6G in 0%, 10%, 20%, 30% and 40% sucrose. (b) Dependence of the diffusion coefficient on viscosity obtained by fitting the previous curves. The diffusion coefficients were determined by calibrating with the literature value of 414 µm²/s for R6G in water [34].

### 3.4 High-throughput FCS

Having demonstrated that it is possible to pool together data from different channels using a simple calibration procedure, we investigated the practical limits of our approach by asking how short an acquisition time was sufficient to obtain reliable fit parameters (diffusion time and concentration) in the conditions used for these experiments. We focused on a typical data set obtained with a 1 nM R6G sample resulting in 12 kHz of average signal above the ~1kHz background (comprised of sample background and detector dark count signal).

In order to assess how quickly meaningful FCS data can be acquired, a fit quality metric is needed. The issue of the signal-to-noise ratio in FCS being a complex one [35–39], we set an arbitrary criterion of 10% uncertainty of the fit parameters across sequential measurements of the same sample as our lower bound. According to this criterion and Fig. 12, reliable FCS parameters can be obtained with only 1 second of acquisition from 8 channels in parallel.

Figure 12a illustrates this approach by representing 20 8ch-averaged ACF curves corresponding to different 1 s acquisitions, along with the calibrated ACF curve of a single channel (248 s acquisition). For comparison, 20 single-channel, calibrated ACF curves corresponding to an equivalent 8 seconds of measurement are shown in Fig. 12b. As expected these plots are very similar.

Equivalently, we verified that the standard deviations of the fit parameters (*d* and *n*) obtained from 100 8ch-averaged ACF curves (1 s measurements) were $\sqrt{8}$ smaller than the standard deviations obtained from 100 single-channel ACF curves (1 s measurements).
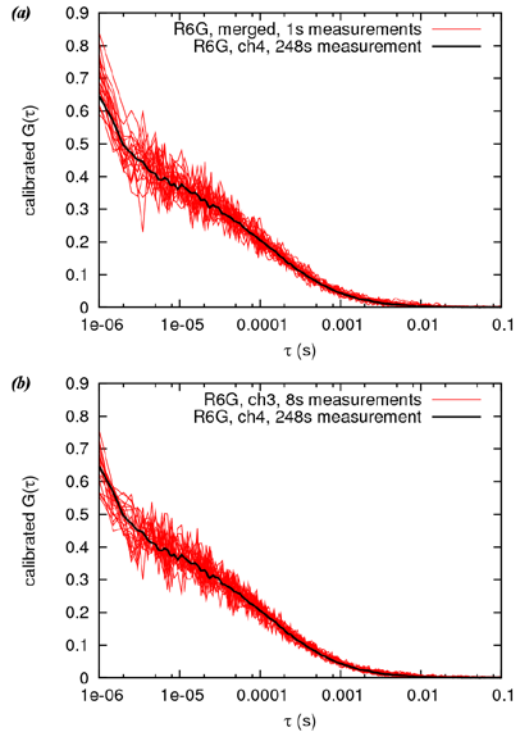
Fig. 12. FCS curves obtained from many short acquisitions of (a) 1s and (b) 8s each, with the curves showing (a) merged acquisitions from all channels, and (b) acquisition from a single channel, with comparison to the full 248 second acquisition from a single channel.

## 4. Discussion

The previous results demonstrate the basic high-throughput FCS capabilities of our optical setup. It is based on three innovations: (i) a programmable LCOS-SLM used in real space to generate a multispot excitation pattern, (ii) a monolithic linear SPAD array and (iii) a parallel data acquisition board based on an FPGA.

### 4.1 LCOS-SLM

The "direct space" approach used to program the LCOS-SLM has several advantages over the standard "Fourier space" or spatial-frequency approach used in holography. In particular, it allows a straightforward and instantaneous implementation of arbitrary patterns (number, size and geometrical arrangements and orientation) of spots by using the principle of Fresnel lens construction. Although some constraints are imposed on the LCOS pattern by electric field bleed-through from pixel to pixel and by diffraction, this approach affords great flexibility to adapt the setup to different experimental situations. In particular, it was critical to be able to slightly adjust the orientation of the pattern to achieve a perfect alignment with the detector. This was achieved by modifying the pattern inclination using a simple user interface and validating the alignment by live monitoring of the recorded count rate.

Aside from the flexibility gained by rapid pattern computation, the direct space approach has some experimental advantages which are important for this application. With a spatial-frequency approach to forming spots, the resulting position of each spot is sensitive to the flatness of the phase of the incident plane wave across the entire pattern area, which can make alignment much more challenging. Using the direct space approach, the spot positions are only sensitive to the flatness of the phase of the plane wave across the subset of the pattern which is responsible for each spot, which is much flatter due to it being a much smaller region

of the incident light. In contrast, the direct space approach suffers from more intensity non-uniformity for the same reason, in that the intensity of each spot is determined by only a localized region, and thus spots near the periphery have less intensity. As correct alignment is more critical to this application than intensity uniformity, this provides additional support for choosing the more computationally efficient direct space approach.

In Figs. 5 and 6 the PSFs obtained for a linear array of 8 spots were shown. By simply changing the parameter for the number of spots in the LCOS control software, a square array of 8x8 spots can be created with similar characteristics to the linear array of 8. We have found that the total number of spots can be readily increased to 32x32 using this approach (data not shown). However, increasing the number of spots introduces some complications. In particular, we observed a noticeable increase in out of focus light and increased aberrations and alignment challenges for spots away from the center. It also makes it challenging to obtain both sufficient power per spot and uniform excitation over the whole LCOS area (data not shown).

The detector pattern comprised eight SPADs (radius $r_E = 25$ μm) separated by $d_E = 250$ μm. The LCOS pattern pitch was therefore entirely defined by: 1) the detection path magnification, $M$, 2) the desired spot separation in the sample focal plane, $d_X$, and 3) the excitation path magnification, $m$.

Optical parameters for the excitation path were chosen such that the excitation spots were almost diffraction-limited in the sample focal plane (Fig. 6). The Gaussian waists of the spots, $w_{xy}$, are given by:

$$w_{xy} \sim 0.42 \frac{\lambda}{NA} , \tag{18}$$

where $\lambda = 532$ nm is the excitation wavelength and $NA = 1.2$ the numerical aperture of the objective lens. Next, to ensure that each measurement was temporally and spatially decoupled from one another, we had to impose:

$$d_X \gg w_{xy} . \tag{19}$$

Finally, in order to ensure proper rejection of out-of-focus light, the magnification $M$ needed to be chosen such that the detector sensitive area acted as a pinhole of dimension comparable to that of the excitation spot image:

$$M \sim \frac{r_E}{w_{xy}} , \tag{20}$$

imposing:

$$d_X = \frac{d_E}{M} \sim \frac{d_E}{r_E} w_{xy} . \tag{21}$$

Since by design of the detector $d_E/r_E = 10$, Eq. (19) follows from Eq. (21). We used a magnification $M \sim 55$ and $d_X \sim 4.5$ μm, close to ideal conditions for out-of-focus rejection ($r_E/w_{xy} = 66$). The magnification $m = 1/89$ was set to match the LCOS pattern pitch ($20 \times 20$ μm = 400 μm) to the desired $d_X$. Any other detector design or sample excitation pattern could have been easily accommodated by adjusting the LCOS pattern and/or the excitation/emission paths magnifications.

In particular, for applications requiring larger separations between the excitation volumes, such as when using microfluidic devices to dispense different samples into neighboring excitation volumes, the excitation path magnification and LCOS pattern can be adjusted to increase the spot separation while preserving the diffraction-limited size of the spot.

## 4.2 SPAD array

A cornerstone for building a high-throughput and high-performance FCS setup is provided by the SPAD array detector, which is implemented using a custom technology that guarantees high photon detection efficiency and low dark current in every pixel. It is possible to use the experiences gained from an FCS setup using this type of detector to guide the development of new detectors with features tailored to specific requirements of single molecule spectroscopy, such as a different spectral response, different detector geometries, and different numbers of pixels. For example, a square geometry (8x8) would enable a substantial increase in pixel number while still covering a similar radial distance outward from the center of the excitation pattern. Also, increased background rejection could be obtained by designing a detector with built-in pinholes to shrink the effective pixel diameter, which would improve the ratio between pitch and pixel diameter described in Eq. (21).

## 4.3 Data acquisition system

Each SPAD of the array outputs an independent train of 50 ns TTL pulses corresponding to the detected photons. Although multichannel correlator hardware capable of processing up to 32 channels is commercially available, we were interested in developing a flexible data acquisition system providing time-stamping information for each photon and offering the capability to further process this information for future applications. The commercial digital input-output (DIO) boards (PXI-6602, NI) we used in previous applications [40] to record photon-counting data from multiple SPADs are in principle capable of supporting up to 8 independent recording channels, as required for the SPAD array used in this work. However, the sustained throughput of those boards is limited by data transfer to the host computer. Indeed, each recording channel implemented on these boards communicates with the computer via direct memory access (DMA, fast) or interrupts (slow), with a maximum of 3 DMA channels available per computer. In practice, recording data from more than 3 channels simultaneously using this type of hardware may result in data loss.

For these reasons, we decided to use a reconfigurable DIO board based on FPGA hardware. Although we used a specific commercial model (PXI-7813R, NI), similar tasks could be easily accomplished with comparable hardware. The key features of the reconfigurable DIO board we used were the possibility to: (i) manage a large number of independent TTL input channels (up to 160) and (ii) program independent time-stamping tasks for each channel and (iii) use a common (large) data buffer for DMA transfer to the PC using a single DMA channel. The current data throughput limitation (20 MHz) due to the peripheral component interconnect (PCI) communication bus (~100-150MHz) used by the board will be improved once similar hardware using a faster PCI Express communication bus becomes available.

An important advantage of our solution is its potential for real-time on-board data processing (e.g. time-binning) before data transfer to the computer, with the dual advantages of reducing CPU load and reducing data transfer bandwidth.

## 4.4 Future applications

We have chosen to first demonstrate the high-throughput FCS capabilities of this setup because of the relative ease of implementation of this application: a single detection channel per spot is sufficient to obtain the diffusion coefficient and concentration of the sample. In addition, to simplify sample handling, we limited ourselves to observing the same sample in each excitation spot. A natural extension of HT-FCS would consist of combining it with microfluidic sample dispensing technology, in order to observe a different sample in each excitation spot. As discussed previously, our approach would allow straightforward adjustment of the spot geometry to match that of the microfluidic sample holder.

The use of a single SPAD array in the experiments presented here has the disadvantage that SPAD afterpulsing dominates the short time scale behavior of the ACFs (Fig. 4),

preventing one from studying sub-microsecond dynamic phenomena. A standard workaround in single spot FCS is to use a Hanbury Brown & Twiss (HBT) configuration, using two SPADs, each collecting 50% of the emitted signal split by a beam-splitter cube, and computing the cross-correlation function (CCF) of the two detector signals [4]. A high-throughput HBT configuration using two SPAD arrays would be a relatively simple extension of our design, although perfect alignment of the two detectors would present a new challenge. A similar configuration using a dichroic mirror instead of a beam-splitter cube to distinguish photons emitted in different spectral ranges would allow high-throughput two-color fluorescence cross-correlation spectroscopy (FCCS), a powerful extension of FCS with many fundamental and biotechnological applications [5].
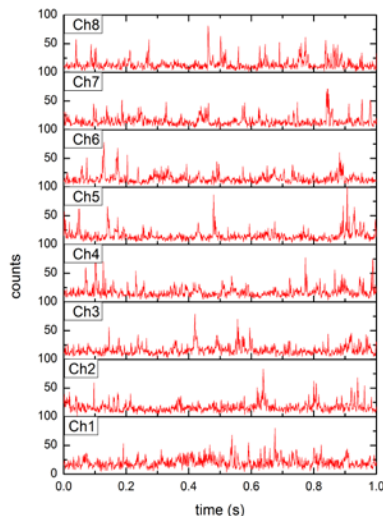


Fig. 13. One second time traces of R6G in 40% sucrose, shown for all 8 channels (1 ms binning). Single-molecule bursts with ~50-100 kHz emission rates are clearly visible.

The current setup is capable of detecting single-molecule bursts in each excitation spot (Fig. 13), enabling high-throughput single-molecule spectroscopy of diffusing molecules. In particular, high-throughput two-color single-molecule detection would allow speeding up the acquisition of single-molecule FRET data, enabling the study of slow varying equilibria [41] or simply increasing the overall throughput of the powerful but still relatively tedious single-molecule fluorescence approaches [1,42].

## 5. Conclusion

We have presented the first high-throughput FCS application of a new custom CMOS single-photon avalanche photodiode array using a liquid crystal on silicon spatial light modulator and a reconfigurable data acquisition board. More generally, this powerful combination of recent technological developments appears extremely promising for high-throughput single-molecule fluorescence spectroscopy.

## Acknowledgments

equations. This work was funded by NIH grant R01-GM084327. Ryan A. Colyer and Giuseppe Scalia contributed equally to this work.